

Characterization of high-velocity impact damage in CFRP laminates: Part I- experiment

Yashiro, Shigeki

Department of Mechanical Engineering, Shizuoka University

Ogi, Keiji

Graduate School of Science and Engineering, Ehime University

Nakamura, Tsukasa

Graduate School of Science and Engineering, Ehime University

Yoshimura, Akinori

Advanced Composite Research Center, Japan Aerospace Exploration Agency (JAXA)

<https://hdl.handle.net/2324/4476060>

出版情報 : Composites Part A: Applied Science and Manufacturing. 48, pp.93-100, 2013-01-18.
Elsevier

バージョン :

権利関係 :



Characterization of high-velocity impact damage in CFRP laminates: Part I– experiment

Shigeki Yashiro ^{a,*}, Keiji Ogi ^b, Tsukasa Nakamura ^c, and Akinori Yoshimura ^d

^a Department of Mechanical Engineering, Shizuoka University

3-5-1 Johoku, Naka-ku, Hamamatsu 432-8561, Japan

^b Graduate School of Science and Engineering, Ehime University

3 Bunkyo-cho, Matsuyama, Ehime 790-8577, Japan

^c Graduate School of Science and Engineering, Ehime University (Currently, NIPPI Corporation)

3 Bunkyo-cho, Matsuyama, Ehime 790-8577, Japan

^d Advanced Composite Research Center, Japan Aerospace Exploration Agency (JAXA)

6-13-1, Osawa, Mitaka, Tokyo 181-0015, Japan

* Corresponding author: Tel: +81-53-478-1026; Fax: +81-53-478-1026.

E-mail address: tsyashi@ipc.shizuoka.ac.jp (S. Yashiro)

Abstract

This study investigated mechanisms of the extension of high-velocity impact damage in CFRP laminates. To this end, damage states due to near-perforation impact were studied in detail. This study consists of two parts. Part I presents the experiment results of high-velocity impact tests for CFRPs with specified stacking sequences. A crater and splits were observed on the impacted surface, while multiple splits with fiber breaks extended on the back surface. The cross-section beneath the impact point included catastrophic ply failure with extensive fiber breaks. Impacted specimens also exhibited a particular delamination pattern consisting

of pairs of symmetric fan-shaped delaminations emanating from to the impact point and elongated delamination along the cracks in the bottom ply. These damage patterns were common to all of the stacking sequences. Part II of this study presents a numerical analysis of high-velocity impact based on smoothed-particle hydrodynamics and discusses damage extension mechanisms.

Keywords: A. Polymer-matrix composites (PMCs); B. Impact behaviour; B. Delamination; D: Fractography.

1. Introduction

Advanced composite materials such as carbon fiber reinforced plastics (CFRPs) have been frequently used in various industries because of their superior specific strength and specific stiffness. For example, CFRPs have been applied to primary load-bearing structures like the fuselage and wings in the latest airplanes. In recent years, CFRPs have also been used in turbofan engines. One problem with these engines is failure of the engine system caused by high-velocity impact of foreign objects such as small stones and birds. When a fan blade breaks and flies apart, the fan case should bear the impact of the fan blade. Therefore, understanding the mechanisms of foreign object damage in composite materials is essential for improving the tolerance and reliability against impact at a velocity near the speed of sound in air.

Delaminations are frequently generated in composite laminates due to out-of-plane impacts, and many experiments and analytical studies on low-velocity impact damage [1-4] have been conducted assuming tool drops. Some studies have also been reported on high-velocity impacts on composite materials. Cantwell and Morton [5-7] investigated the low and high velocity impact response of CFRP laminates. A series of experiments revealed that the

projectile generated a localized deformation state under high-velocity impact loading, which was opposite of the low-velocity cases. They also demonstrated that fast-moving projectiles induced a localized target response and most of the incident energy was then dissipated over a small area adjacent to the impact point; therefore, for a given impact energy, decreasing projectile mass (increasing impact velocity) resulted in greater levels of damage. A conical-shaped shear-out fracture zone was observed in the cross-sections regardless of the stacking sequence, and a simple perforation model to predict the perforation threshold energy was developed and verified.

Recent experiment studies [8-13] mainly discussed the energy required for perforation and energy absorption due to damage extension. López-Puente et al. [8] investigated the delamination area and its temperature dependence in woven CFRP laminates and quasi-isotropic CFRP laminates. They demonstrated that the delamination area was constant over a large velocity range. Tanabe et al. [9] studied laminates made of different reinforcing fibers and concluded that the mechanical properties of the rear layer play an important role for energy absorption and that a laminate with lower interlaminar shear strength effectively absorbed the impact energy. Hazell et al. [10,11] investigated the influence of the impact velocity and determined that the energy absorption accompanied by damage extension was constant for high- to hyper-velocity impacts. Appleby-Thomas et al. [12] carried out ice impact tests with CFRPs assuming a hail storm and studied the projected damage area and the CAI strength. Shimamoto et al. [13] studied impact response at cryogenic temperatures and concluded that the stacking sequence played an important role to control the damaged region of a main space structure. Furthermore, the recent advances in experimental studies on high-velocity impacts of composite materials have been summarized in the latest reviews [14,15]. Wen [16] and López-Puente et al. [17] proposed theories to predict the ballistic limit velocity

by considering the energy balance and the energy dissipation due to damage extension. These theories were compared with experiment results and were verified [16-18]. Numerical studies using finite-element analysis on the impact response of composite plates have also been reported. Gower et al. [19] analyzed the ballistic impact of an AFRP laminate and obtained reasonable agreement with the experiment results for back-surface displacement and delamination. He et al. [20] used only a projectile model to predict the penetration depth and the ballistic limit, assuming that the response of the target was a function of the impact velocity. López-Puente et al. [21] successfully predicted the projected damage area in CFRP woven laminates due to normal and oblique ballistic impacts.

The extension mechanisms of complex impact damage in composite laminates must be understood to improve the reliability of composite structures, because such impact damage severely degrades residual strength. However, the final goal of the studies on high-velocity impact response of composite materials is applications such as space debris bumper shields and armor, so previous studies on high-velocity and hyper-velocity impacts (e.g., Refs. [22,23]) focused on the perforation and the ballistic limit, and there have been few detailed discussions of the various kinds of damage in plies and at ply interfaces. Characterization of the extension of high-velocity impact damage is valuable for clarifying the energy absorption mechanisms and eventually the ballistic limit.

This study therefore sought to characterize high-velocity impact damage in CFRP laminates and to clarify its extension mechanism. To this end, we focus on damage states caused by near-perforation impacts. This study consists of two parts. Part I conducts high-velocity impact tests on CFRP laminates with four basic stacking sequences, namely a unidirectional laminate, two cross-ply laminates, and a quasi-isotropic laminate, and presents detailed observations of the resulting impact damage using optical microscopy and soft X-ray

radiography. Part II will analyze the extension of impact damage in CFRP laminates based on smoothed-particle hydrodynamics (SPH) and will discuss the mechanism of damage extension.

2. Materials and procedure

Carbon-fiber-reinforced epoxy prepreg sheets (T700S/#2521R, Toray Industries) were used, and the laminates were manufactured by heating and pressing the stacked sheets in a vacuum chamber. The stacking sequences were unidirectional $[0_{16}]$ (UD), cross-ply $[0_4/90_4]_s$ (CP1), cross-ply $[0/90]_{4s}$ (CP2), and quasi-isotropic $[0/45/90/-45]_{s2}$ (QI). The fiber direction in the top and bottom plies was defined as the 0° direction. The prepared laminates were cut into square specimens 55 mm on a side and 1.6 mm thick. Although the size of the target may be small, the areal dimensions could have little influence on the high-velocity impact response, and small-scale specimens were sufficient to reproduce the damage states in large structures [24]. The specimen thickness may also be small for typical applications, but thin specimens were employed to discuss near-perforation damage using our impact testing machine.

Figure 1 schematically depicts a high-velocity impact testing machine (Maruwa Electronic Incorporated). This machine consists of a control unit for the power source, a chamber in which a projectile was shot at a target, and a speed detector with a data logger. The projectile, set in a sabot, was accelerated with high-temperature, high-pressure metal plasma obtained by melting and evaporating an aluminum foil subjected to high-voltage pulse current. The sabot was stopped at the mouth of the gun, and the sphere moved ahead by inertia. The velocity of the projectile was variable from 40 to 1500 m/s. The velocity was controlled by the voltage applied to the aluminum foil and was precisely measured by obtaining the time required for the projectile to pass the prescribed distance (250 mm) in the speed detector. Only the four

edges of the specimen were fixed to a square-frame jig, and therefore bending due to impact was permitted. The projectile was a steel ball 1.5 mm in diameter (14.2 mg in mass), and the impact velocity was 300 to 1200 m/s. The tests were conducted in an atmospheric environment.

After the test, the damage patterns on the front and back surfaces of the specimen were observed by a stereomicroscope. The specimen was then cut and polished to facilitate observing the damage beneath the impact point by an optical microscope. Internal damage in some specimens was nondestructively imaged by soft X-ray radiography.

3. Experiment results

3.1 Impact damage on the front and back surfaces

Figures 2-5 depict the damage patterns on the front surface and the back surface at specified impact velocities. None of the specimens were penetrated by the projectile, despite severe damage on the back surfaces. The front surfaces of all of the specimens had a crater with splits extending from the crater edges. This damage pattern appeared regardless of the stacking sequence and the impact velocity. The back surfaces had fiber breaks due to the indentation of the projectile and the accompanying splits; this pattern was observed in all four stacking sequences. Splits on the back surface in the UD laminate were generated at a lower velocity (437 m/s) than in the other laminates because of its low bending stiffness in the transverse direction. The fiber breaks on the back surface exhibited the zigzag pull-out patterns that can be seen on tensile fracture surfaces, so it was determined that the bending-induced tensile stress along the fiber direction caused fiber breaks on the back surface.

In order to quantitatively evaluate the influence of the stacking sequence on the external damage, the projected damage area on the surfaces was measured by imaging software; on the

back surface, the damaged region was approximated by several rectangular shapes instead of the projection because of the large out-of-plane deformation. Figure 6 plots the projected damage area against the impact velocity. The damage area on the front surface increased with increasing velocity. This trend was most prominent in the QI laminate, followed by the CP1 and CP2 laminates. However, in the UD laminate, the projected damage area was almost constant (5 mm^2) when plotted against the impact velocity. The damage area on the back surface increased with increasing impact velocity in all the laminates. This increasing trend was significant in the QI and CP2 laminates, and the damage area of the CP1 laminate was always smaller than that of the CP2 laminate. Although the increasing trend also appeared on the back surface of the UD laminate, the growth rate was less than that of the other laminates. The damage area on the front and back surfaces will become constant at higher impact velocities generating a perforation hole [9,25].

The bending stiffness was calculated by classical lamination theory assuming that bending deformation due to the impact contributes to the damage extension on the back surface, although the high-velocity impact induces local bending deformation [4,5], and thus a simple discussion is difficult. Bending stiffness components D_{11} and D_{22} are listed in Table 1, where the longitudinal Young's modulus is 140 GPa, the transverse Young's modulus is 10 GPa, the in-plane Poisson's ratio is 0.35, and the in-plane shear modulus is 5 GPa. Here, subscripts 1 and 2 represent the longitudinal direction and the transverse direction in the 0° ply. In the UD and CP1 laminates, the D_{22} component is much smaller than the D_{11} component, and the curvature in the transverse direction of the 0° ply is larger than that in the longitudinal direction. Combined with the anisotropy of the strengths, the fiber-break region becomes small and matrix cracks extend significantly. The above discussion can be confirmed by the observation of the full cross-sections of these laminates (Fig. 7). In the cross-section normal

to the 0° direction whose top and bottom layers are transverse plies, the small bending stiffness caused severe local bending deformation, which resulted in extensive matrix cracks in the bottom layer (Figs. 7a and 7c). However, this deformation of the CP1 laminate was smaller than that of the UD laminate because of the smaller difference between the D_{11} and D_{22} components. This reduced matrix cracks but induced fiber breaks in the bottom layer (Fig. 7d). The D_{22} component is much balanced with the D_{11} component in the CP2 and QI laminates, and the bending deformation becomes less than that in the transverse direction of the other two laminates. Many fiber breaks are then generated due to the indentation of the projectile. Further indentation expands the fiber-break region and peeling off of the bottom ply, which causes matrix cracks in the back surface. Therefore, the CP2 and QI laminates have a larger damage area on the back surface than the UD and CP1 laminates because of the extensive fiber breaks.

3.2 Damage state beneath the impact point

Two cross-sections including the impact point were observed by an optical microscope. One is a cross-section normal to the fiber direction of the 0° ply (N-section); the other is a cross-section parallel to that direction (P-section).

Figure 8 depicts the damage state beneath the impact point in the UD laminate. A crater, delaminations, and oblique matrix cracks appeared in the N-section (Fig. 8a). The region just beneath the crater broke catastrophically. Oblique matrix cracks (i.e., cone cracks) were generated outside the catastrophic failure zone and were connected with delamination. In the bottom ply, a matrix crack connected to the ply failure zone had a large opening distance due to severe bending deformation. The crater and delaminations were also observed in the P-section (Fig. 8b). The fibers seemed to be cut by out-of-plane shear deformation at the crater

edge. The P-section delamination had a larger opening displacement than the N-section, and therefore the delamination extended extensively toward the fiber direction.

Figure 9 depicts the damage state beneath the impact point in the CP1 laminate. A crush region (i.e., a crater) in the top 0° plies, fiber breaks and delamination in the 90° plies, and matrix cracks in the bottom 0° plies were observed in the N-section (Fig. 9a). The fiber breaks and delaminations in the 90° plies induced easy deformation of the bottom 0° plies, and matrix cracks were then generated in the bottom plies. A crater with fiber breaks, a catastrophic ply-failure zone, cone cracks, and delaminations were observed in the P-section (Fig. 9b), where the four bottom 0° plies were delaminated and dropped off. Considering fiber breaks in 90° plies beneath the impact point in the N-section, the catastrophic ply-failure zone was found to include extensive fiber breaks, matrix cracking, matrix crushing, and delaminations. Cone cracks and delaminations outside the catastrophic ply failure zone in the 90° plies were similar to those observed in the N-section of the UD laminate (Fig. 8b).

The damage patterns beneath the impact point in the CP2 laminate are depicted in Fig. 10. A crater, fiber breaks, matrix cracks (cone cracks), and delaminations were observed in both the N- and the P-sections. Some matrix cracks were generated in a single ply, with their tips connected to delamination that occurred only at the $0^\circ/90^\circ$ ($90^\circ/0^\circ$) interfaces in the N- (P-) section. More specifically, the upper (lower) ply of delamination was always the transverse (longitudinal) ply. This pattern suggested that the delamination extended from a catastrophic ply failure such as matrix cracking in the transverse ply. Although oblique matrix cracks were generated in every transverse ply, these cracks did not make straight cone cracks beyond the longitudinal plies due to the severe delamination.

Figure 11 depicts the P-section including the impact point for the QI laminate, although both the top and bottom plies had dropped parts. Fiber breaks, delaminations, and matrix

cracks in off-axis plies were observed, and there was no well-defined cone crack because of extensive delamination. Most of the ply interfaces were delaminated, and the stress concentration just beneath the impact point was reduced. This dissipated the impact energy and prevented damage progress in each ply, and thus a small catastrophic ply failure zone was formed.

3.3 Soft X-ray radiography

Typical soft X-ray photographs of the four laminates are presented in Fig. 12. The UD laminate exhibited delamination elongated in the fiber direction, while the delamination was small in the transverse direction. Delaminations observed near the impact point in the CP1 laminate could be separated into two delaminations since there were two ply interfaces. One was a delamination at the upper $0^\circ/90^\circ$ ply interface that was connected to the matrix cracks in the top 0° plies and extended in the transverse direction. The other was a pair of fan-shaped delaminations along the matrix crack in the bottom 0° plies that were symmetric about the impact point. Multiple fan-shaped delaminations near the impact point and elongated delamination accompanied by a matrix crack in the bottom ply were observed in the CP2 and QI laminates.

The fan-shaped delaminations were symmetric about the impact point in all of the stacking sequences except for the UD laminate. This delamination pattern was the same as that observed in the laminates subjected to low-velocity impact [26-28]. The delamination at the lowest interface extended along the matrix cracks (splits in Figs. 2-5) in the bottom 0° ply. These results indicate that delamination caused by high-velocity impact consisted of fan-shaped delaminations covering the region between the matrix cracks in two neighboring plies and elongated delamination along the matrix cracks in the bottom ply, and that this

delamination pattern was independent of the stacking sequences.

Figure 13 plots the projected area of the internal damage, mostly delaminations, against the impact velocity. The delamination area gradually increased with increasing velocity (< 350 m/s) and steeply increased at a velocity within 350-500 m/s. Small but visible damage (i.e., fiber breaks) appeared on the back surface at that velocity range, and this observation suggested that the impact energy could be dissipated mostly by delamination extension, not by fiber breaks. The projected delamination area was approximately constant with impact velocity over 500 m/s (several kJ of impact energy). This trend was observed in all of the stacking sequences, but the constant values differed among them. This result agreed with the observations of specimens perforated by high-velocity impact [8,11] and was in contrast to the low-velocity cases [27,29]. For low-velocity impacts or quasi-static indentations, the energy of indentation was absorbed by delamination extension caused by global deformation. The bending deformation was localized by increased impact velocity, and the energy absorption mechanism then changes from delamination to fiber breaks in the high-strain range [4]. The trend of a constant delamination area indicates that the impact energy was mainly absorbed by fiber breaks in the crater and the catastrophic ply-failure zone. This discussion suggests that the most important parameter governing the ballistic limit is the fiber strength and that decreased interlaminar toughness may increase the delamination area, the dissipated amount of the impact energy, and finally the ballistic limit velocity (energy). However, additional tests and observations are necessary to confirm this.

4. Conclusions

This study carried out high-velocity impact tests for CFRP laminates whose stacking sequences were unidirectional, two types of cross-ply, and quasi-isotropic. The damage states

near perforation in these laminates were characterized experimentally to understand the mechanisms of high-velocity impact damage. The conclusions are summarized as follows.

1. The damage patterns on the front and back surfaces were identical among the four stacking sequences and were independent of the impact velocity. A crater with fiber breaks and multiple splits at both edges of the crater were generated on the front surface of the laminates. Multiple matrix cracks extended on the back surface, and fibers broke just beneath the impact point due to the high impact velocity.
2. The projected surface damage area increased with increasing impact velocity (energy) for all of the stacking sequences, but the rate of increase differed among them. The damage area on the back surface could be determined by the bending stiffness. A low bending stiffness induced a large bending deformation and matrix cracks on the back surface, which resulted in a small damage area. A high bending stiffness caused many fiber breaks beneath the impact point due to the localized high strain. These fiber breaks and the subsequent peeling of the bottom ply resulted in a large damage area.
3. Extensive fiber breaks, which appeared as catastrophic ply failure in the off-axis plies, were generated beneath the impact point. Outside the ply failure zone, delaminations extended from the tips of the matrix (cone) cracks.
4. All of the lamination types exhibited a particular delamination pattern consisting of pairs of fan-shaped delaminations that are symmetrical about the impact point and elongated delaminations along the matrix cracks in the bottom ply.

Part II of this study presents a damage-extension simulation of high-velocity impacts on CFRP laminates based on smoothed-particle hydrodynamics (SPH), and the impact response will be analyzed considering detailed damage modes. The extension mechanisms of the high-velocity impact damage will be discussed based on these observations.

Acknowledgments

S. Y. acknowledges the support of the Ministry of Education, Culture, Sports, Science and Technology of Japan under Grants-in-Aid for Scientific Research (Nos. 21360417 and 22760524). The authors would like to express appreciation for technical supports from Mr. Masamichi Nakata and Mr. Takuya Ioka of Ehime University.

Reference

- [1] Richardson MOW, Wisheart MJ. Review of low-velocity impact properties of composite materials. *Compos Part A* 1996; 27:1123-1131.
- [2] Schoeppner GA, Abrate S. Delamination threshold loads for low velocity impact on composite laminates. *Compos Part A* 2000; 31:903-915.
- [3] Johnson AF, Pickett AK, Rozycki P. Computational methods for predicting impact damage in composite structures. *Compos Sci Technol* 2001; 61:2183-2192.
- [4] Breen C, Guild F, Pavier M. Impact of thick CFRP laminates: the effect of impact velocity. *Compos Part A* 2005; 36:205-211.
- [5] Cantwell WJ, Morton J. Comparison of the low and high velocity impact response of CFRP. *Composites* 1989; 20:545-551.
- [6] Cantwell WJ, Morton J. Impact perforation of carbon fibre reinforced plastic. *Compos Sci Technol* 1990; 38:119-141.
- [7] Cantwell WJ, Morton J. The influence of varying projectile mass on the impact response of CFRP. *Compos Struct* 1989; 13:101-114.
- [8] López-Puente J, Zaera R, Navarro C. The effect of low temperatures on the intermediate and high velocity impact response of CFRPs. *Composites Part B* 2002; 33:559-566.

- [9] Tanabe Y, Aoki M, Fujii K, Kasano H, Yasuda E. Fracture behavior of CFRPs impacted by relatively high-velocity steel sphere. *Int J Impact Eng* 2003; 28:627-642.
- [10] Hazell PJ, Kister G, Stennett C, Bourque P, Cooper G. Normal and oblique penetration of woven CFRP laminates by a high velocity steel sphere. *Compos Part A* 2008; 39:866-874.
- [11] Hazell PJ, Cowie A, Kister G, Stennett C, Cooper GA. Penetration of a woven CFRP laminate by a high velocity steel sphere impacting at velocities up to 1875 m/s. *Int J Impact Eng* 2009; 36:1136-1142.
- [12] Appleby-Thomas GJ, Hazell PJ, Dahini G. On the response of two commercially-important CFRP structures to multiple ice impacts. *Compos Struct* 2011; 93:2619-2627.
- [13] Shimamoto A, Kubota R, Takayama K. High-velocity impact characteristic of carbon fiber reinforced plastic composite at low temperature. *J Strain Analysis* 2012; 47:471-479.
- [14] Hazell PJ, Appleby-Thomas GJ. The impact of structural composite materials. Part 1: ballistic impact. *J Strain Analysis* 2012; 47:396-405.
- [15] Appleby-Thomas GJ, Hazell PJ. The impact of structural composite materials. Part 2: hypervelocity impact and shock. *J Strain Analysis* 2012; 47:406-418.
- [16] Wen HM. Predicting the penetration and perforation of FRP laminates struck normally by projectiles with different nose shapes. *Compos Struct* 2000; 49:321-329.
- [17] López-Puente J, Zaera R, Navarro C. An analytical model for high velocity impacts on thin CFRPs woven laminates plates. *Int J Solids Struct* 2007; 44:2837-2851.
- [18] Caprino G, Lopresto V, Santoro D. Ballistic impact behaviour of stitched graphite/epoxy laminates. *Compos Sci Technol* 2007; 67:325-335.
- [19] Gower HL, Cronin DS, Plumtree A. Ballistic impact response of laminated composite

- panels. *Int J Impact Eng* 2008; 35:1000-1008.
- [20] He T, Wen HM, QIN Y. Finite element analysis to predict penetration and perforation of thick FRP laminates struck by projectile. *Int J Impact Eng* 2008; 35:27-36.
- [21] López-Puente J, Zaera R, Navarro C. Experimental and numerical analysis of normal and oblique ballistic impacts on thin carbon/epoxy woven laminates. *Compos Part A* 2008; 39:374-387.
- [22] Tennyson RC, Lamontagne C. Hypervelocity impact damage to composites. *Compos Part A* 2000; 31:785-794.
- [23] Numata D, Ohtani K, Anyoji M, Takayama K, Togami K, Sun M. HVI tests on CFRP laminates at low temperature. *Int J Impact Eng* 2008; 35:1695-1701.
- [24] Cantwell WJ. The influence of target geometry on the high velocity impact response of CFRP. *Compos Struct* 1988; 10:247-265.
- [25] Fujii K, Aoki M, Kiuchi N, Yasuda E, Tanabe Y. Impact perforation behavior of CFRPs using high-velocity steel sphere. *Int J Impact Eng* 2002; 27:497-508.
- [26] Saito H, Kimpara I. Evaluation of impact damage mechanism of multi-axial stitched CFRP laminate. *Composites Part A* 2006; 37:2226-2235.
- [27] Hull D, Shi YB. Damage mechanism characterization in composite damage tolerance investigations. *Compos Struct* 1993; 23:99-120.
- [28] Aymerich F, Meili S. Ultrasonic evaluation of matrix damage in impacted composite laminates. *Compos Part B* 2000; 31:1-6.
- [29] Nishikawa M, Okabe T, Takeda N. Numerical simulation of interlaminar damage propagation in CFRP cross-ply laminates under transverse loading. *Int J Solids Struct* 2007; 44:3101-3113.

Figure and Table captions

Fig. 1 Schematic diagram of the high-velocity impact testing machine with an electric-heat gun.

Fig. 2 Damage states on the front and back surfaces of the UD [0₁₆] laminates.

Fig. 3 Damage states on the front and back surfaces of the CP1 [0₄/90₄]_s laminates. A barely visible matrix crack was observed on the back surface at 217 m/s.

Fig. 4 Damage states on the front and back surfaces of the CP2 [0/90]_{4s} laminates. Barely visible damage appeared on the back surface at 378 m/s.

Fig. 5 Damage states on the front and back surfaces of the QI [0/45/90/-45]_{s2} laminates. Barely visible damage appeared on the back surface at 480 m/s.

Fig. 6 Relationship between the projected damage area on the front and back surfaces and the impact velocity.

Fig. 7 Full cross-sections of the impacted UD and CP1 specimens.

Fig. 8 Damage states beneath the impact point of the UD [0₁₆] laminate. Impact velocities were 760 m/s for the normal cross-section and 530 m/s for the parallel cross-section.

Fig. 9 Damage states beneath the impact point of the CP1 [0₄/90₄]_s laminate. Impact velocities were 508 m/s for the normal cross-section and 600 m/s for the parallel cross-section. The 0° plies on the back surface peeled off due to extensive delamination.

Fig. 10 Damage states beneath the impact point of the CP2 [0/90]_{4s} laminate. Impact velocities were 500 m/s for the normal cross-section and 700 m/s for the parallel cross-section.

Fig. 11 Damage states in the parallel cross-section including the impact point of the QI [0/45/90/-45]_{s2} laminate. The impact velocity was 707 m/s.

Fig. 12 Soft X-ray photographs of the impacted specimens. Fan-shaped delaminations and elongated delamination along the matrix cracks in the bottom ply were generated.

Fig. 13 Projected delamination area of the UD and CP1 laminates against the impact velocity.

Table 1 Bending stiffness calculated using classical lamination theory.

Table 1 Bending stiffness calculated using classical lamination theory.

Stacking configuration	D_{11} (N m)	D_{22} (N m)
UD $[0_{16}]$	48.2	3.4
CP1 $[0_4/90_4]_s$	42.6	9.0
CP2 $[0/90]_{4s}$	30.0	21.6
QI $[0/45/90/-45]_{s2}$	23.6	18.4

Figure(s)

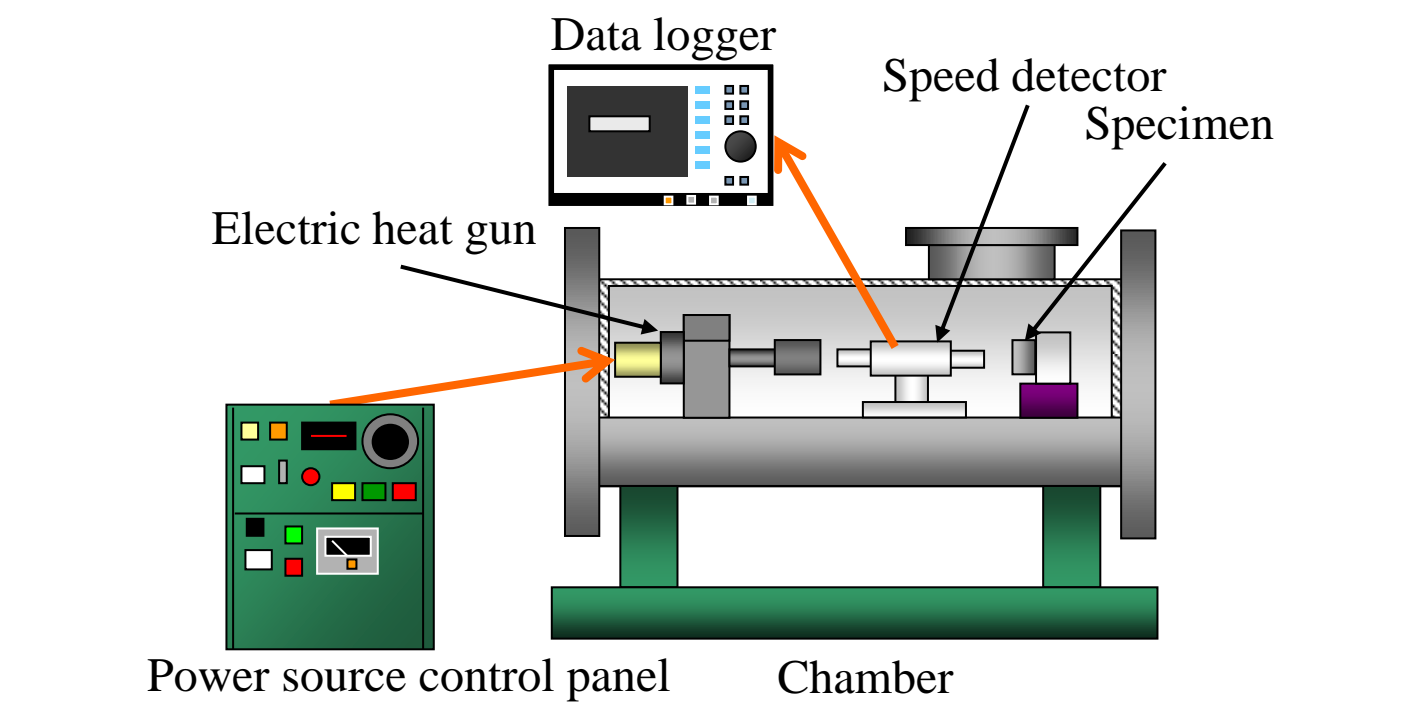


Fig. 1

Figure(s)

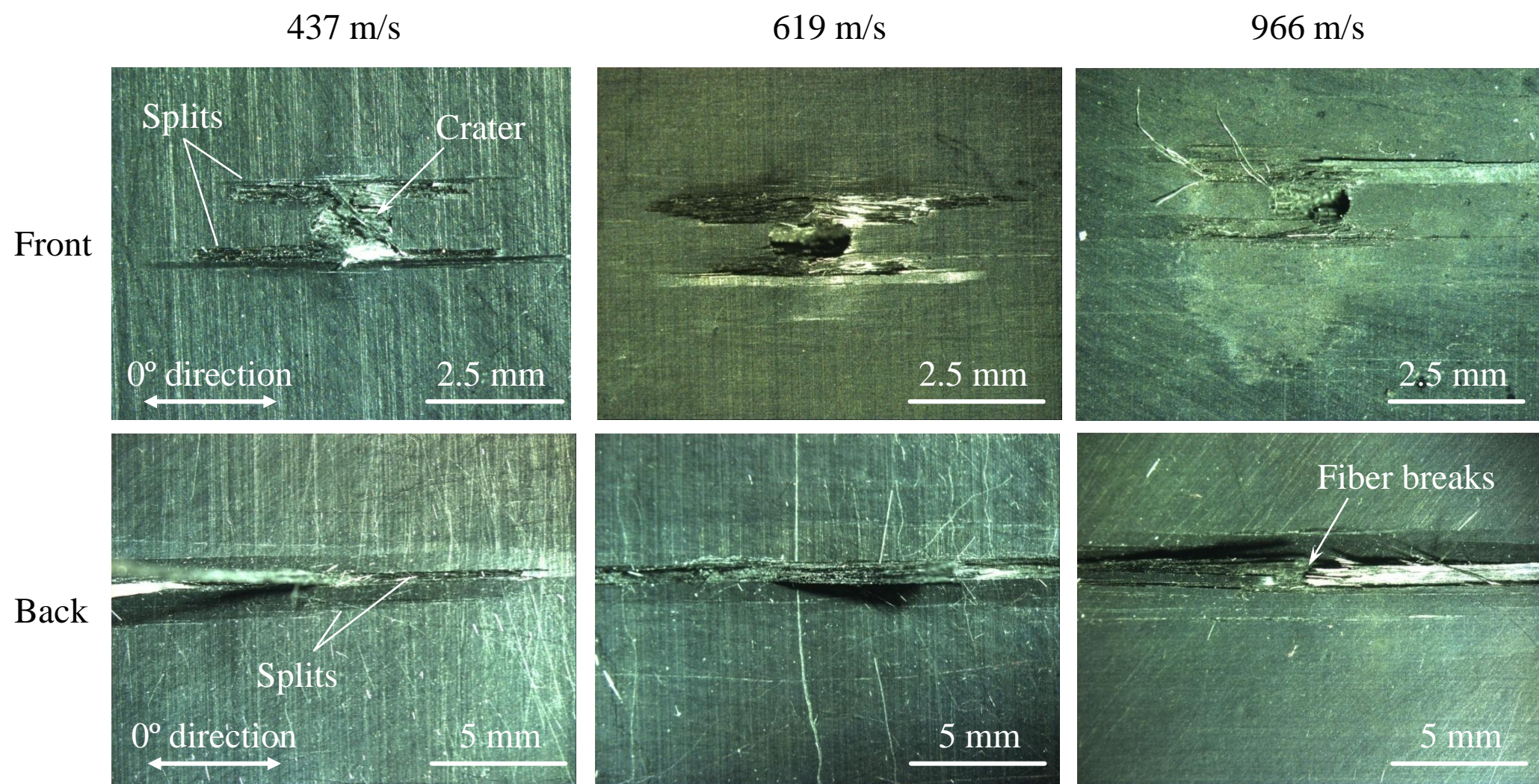


Fig. 2

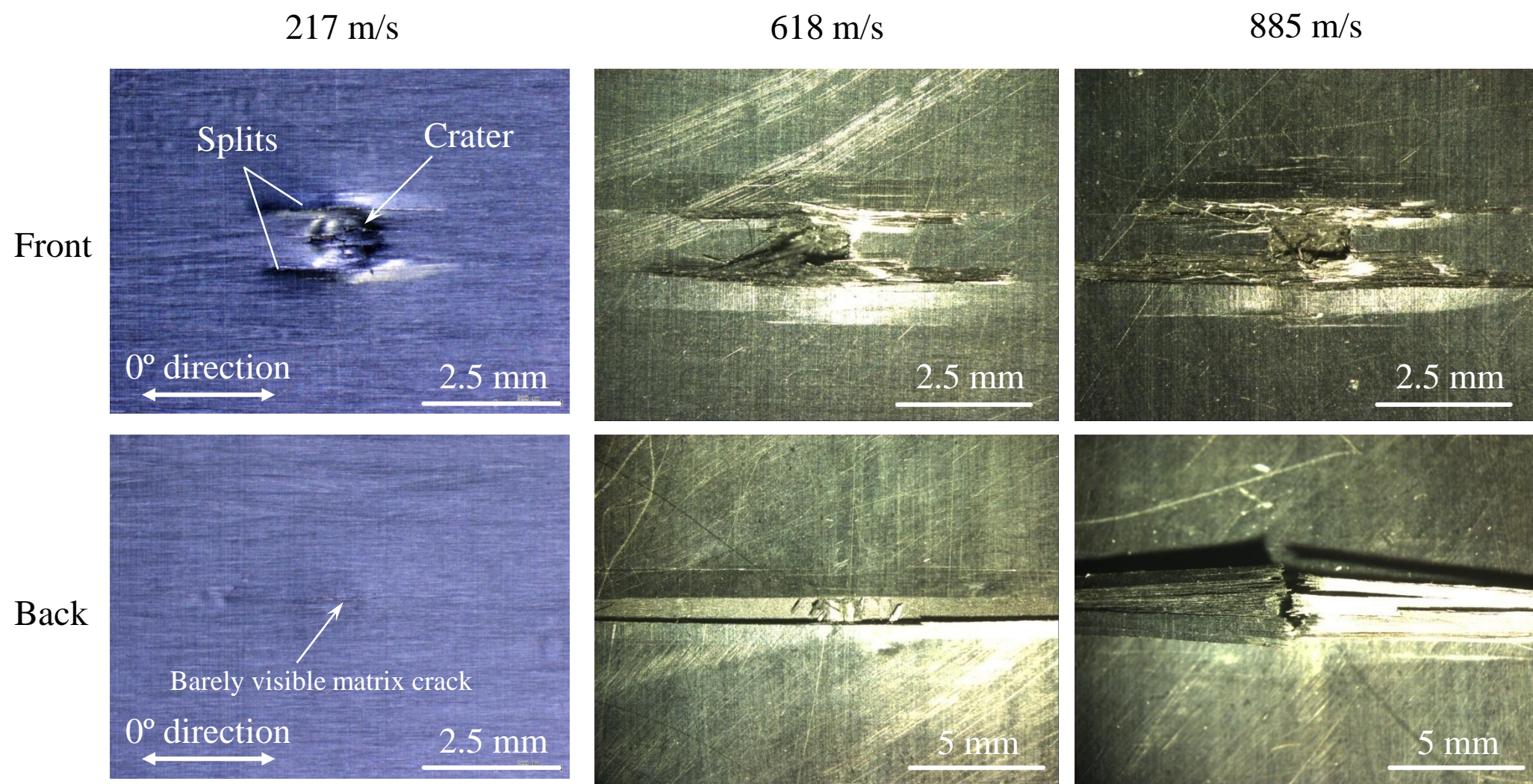


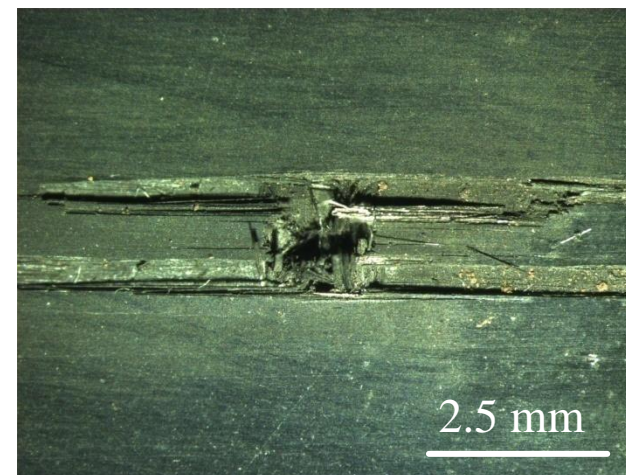
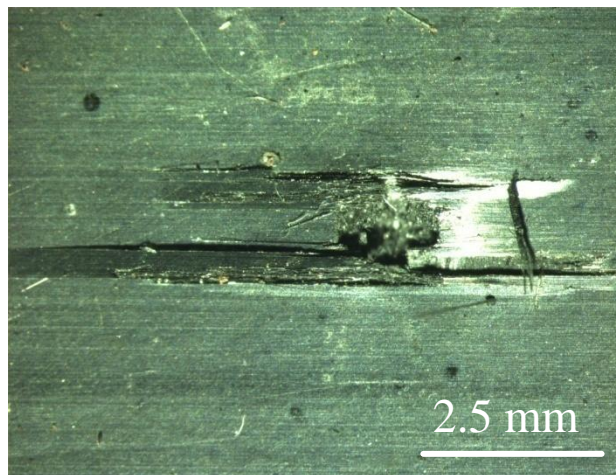
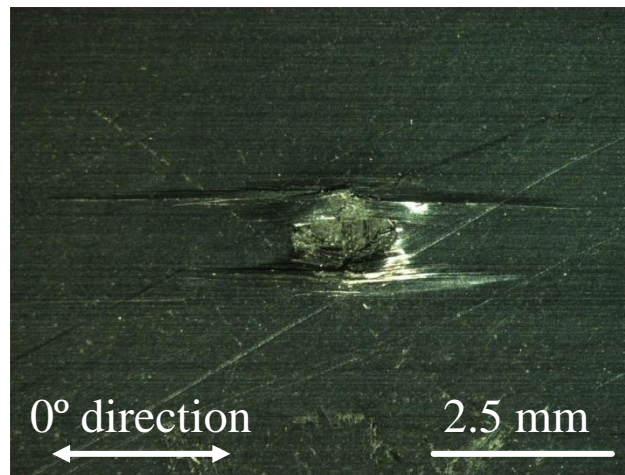
Fig. 3

378 m/s

666 m/s

843 m/s

Front



Back

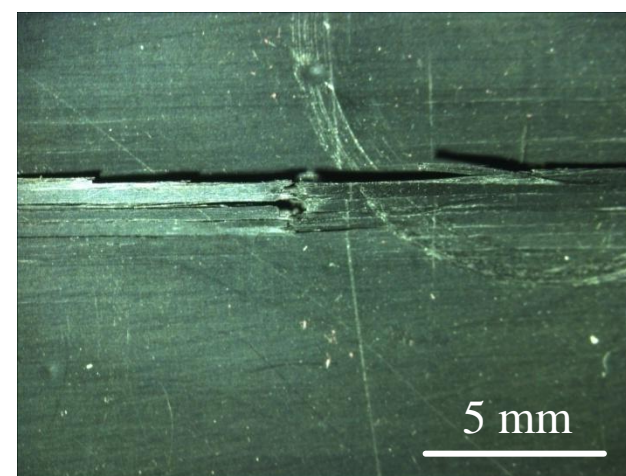
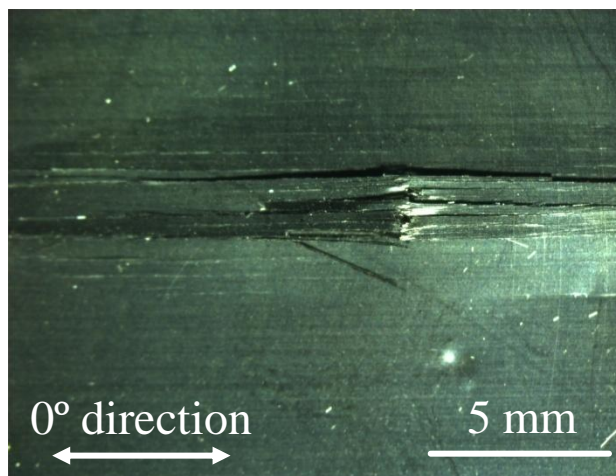
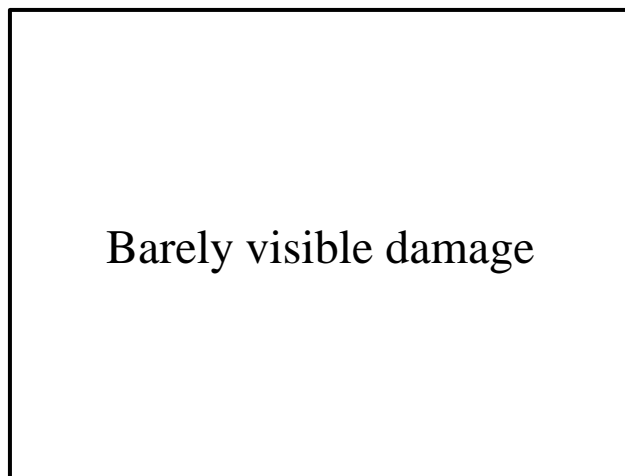


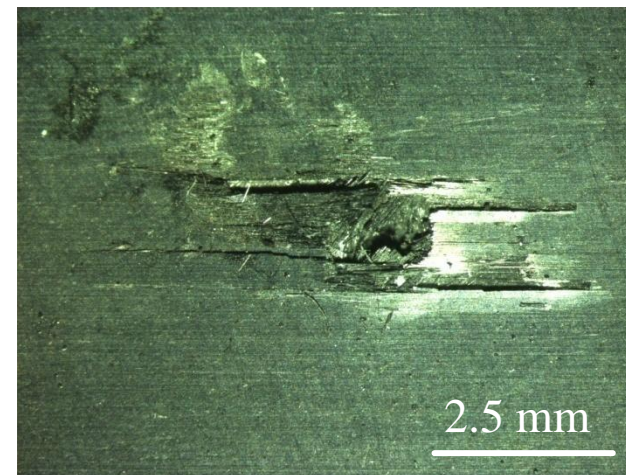
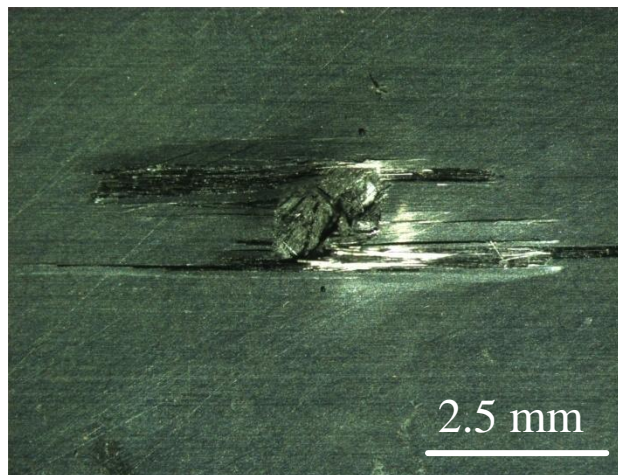
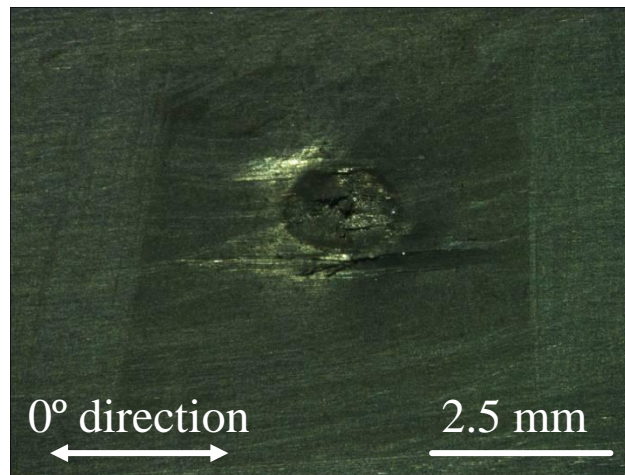
Fig. 4

480 m/s

559 m/s

867 m/s

Front



Back

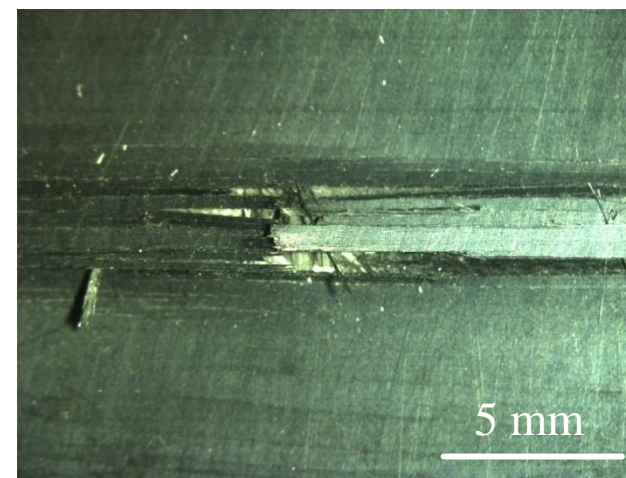
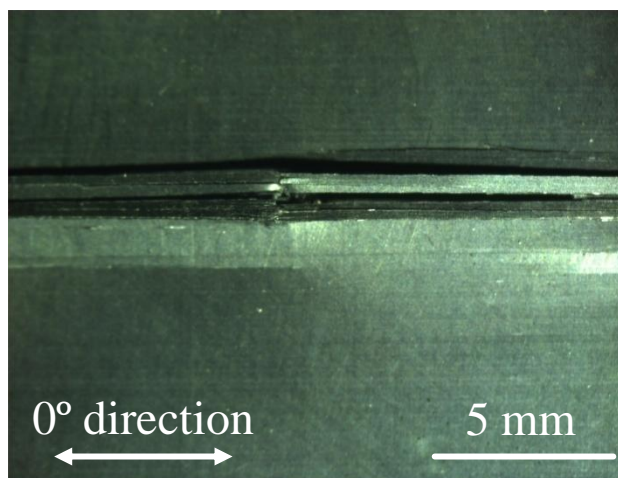
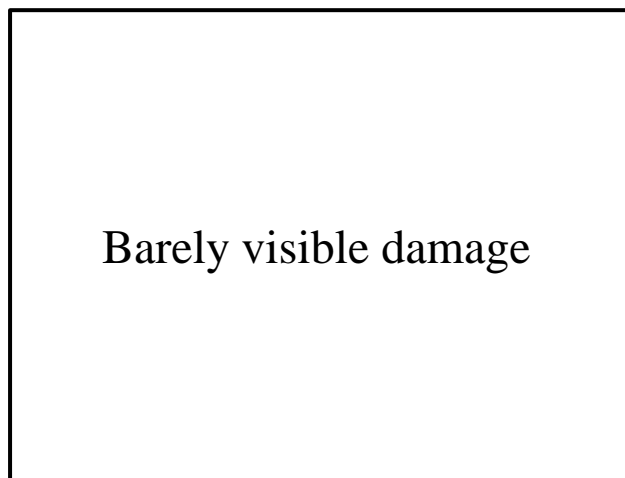
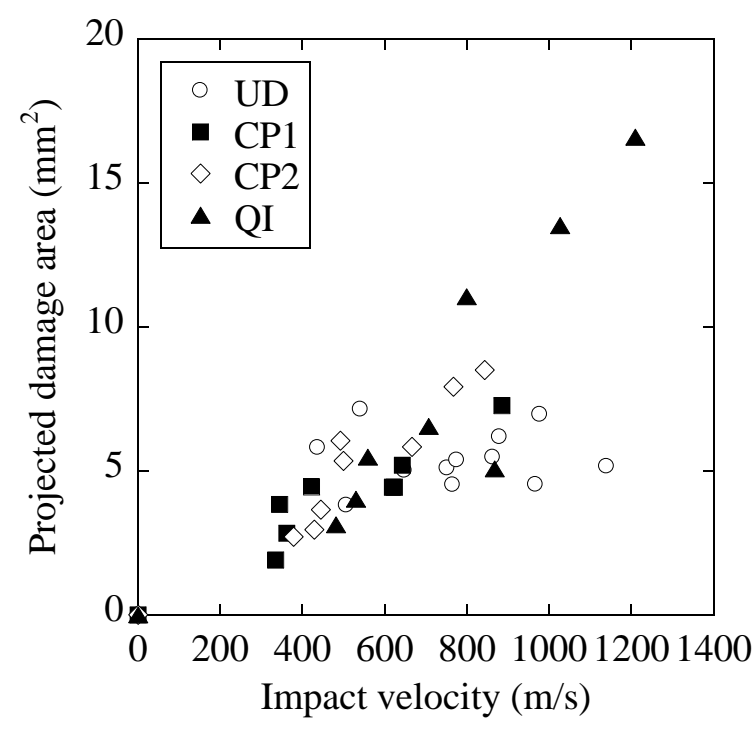
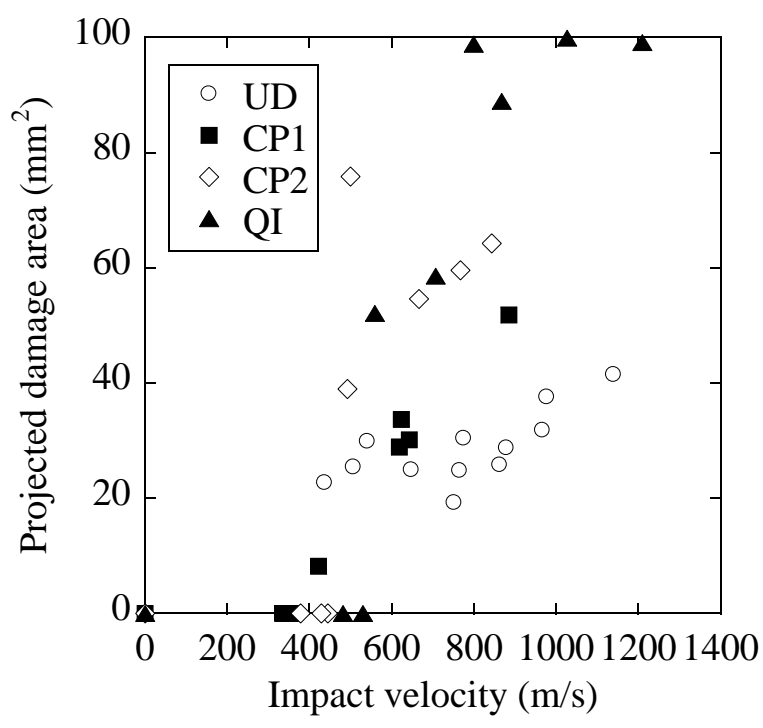


Fig. 5

Figure(s)

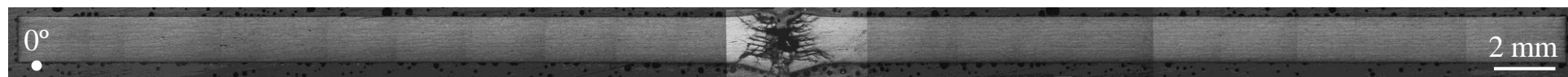


(a) Front surface

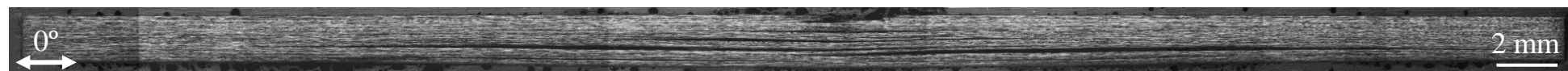


(b) Back surface

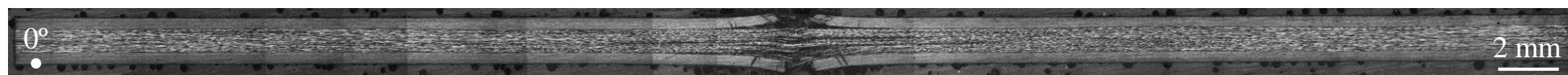
Fig. 6



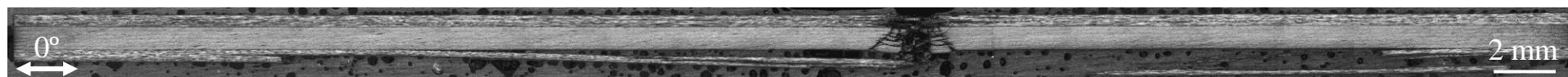
(a) UD (563 m/s), Normal to the 0° direction



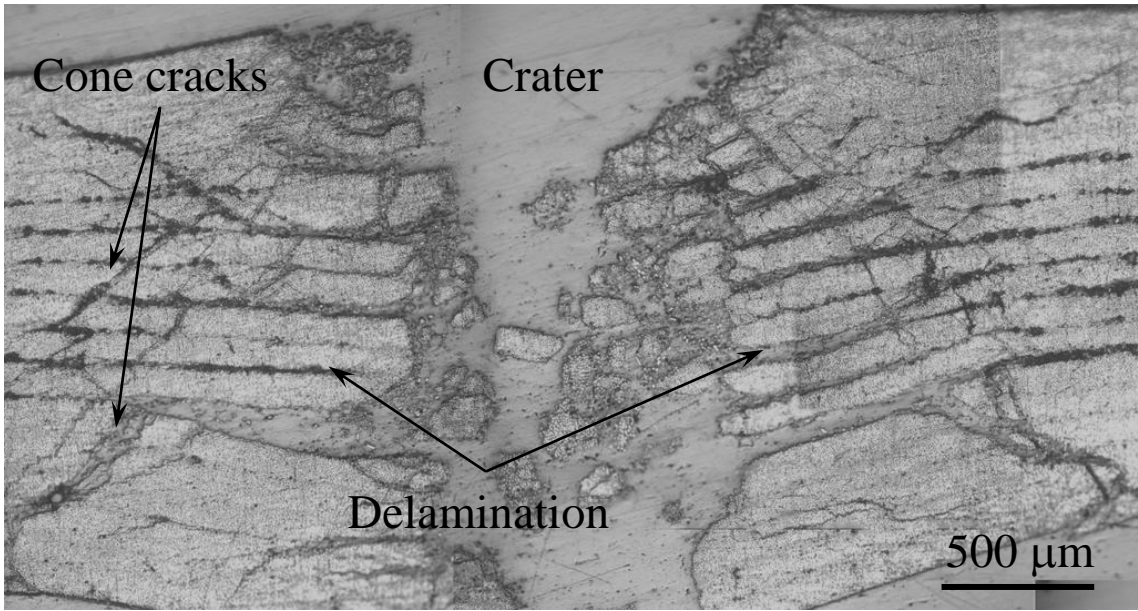
(b) UD (550 m/s) , Parallel to the 0° direction



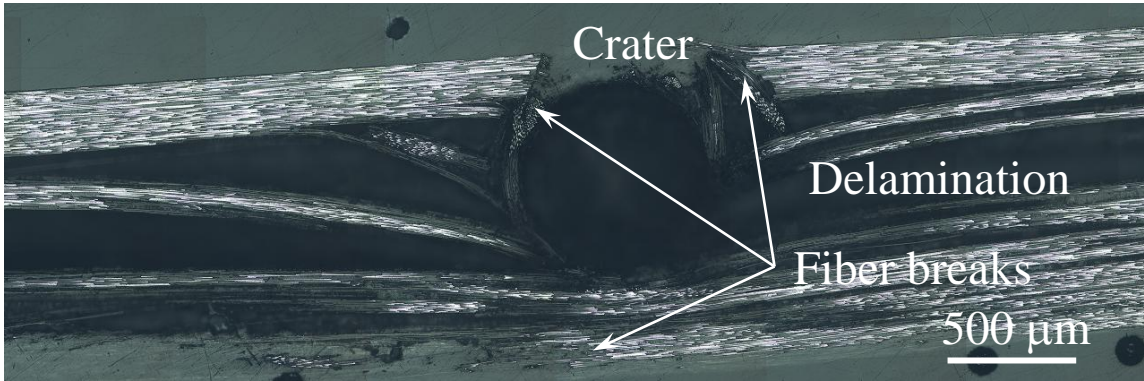
(c) CP1 (531 m/s) , Normal to the 0° direction



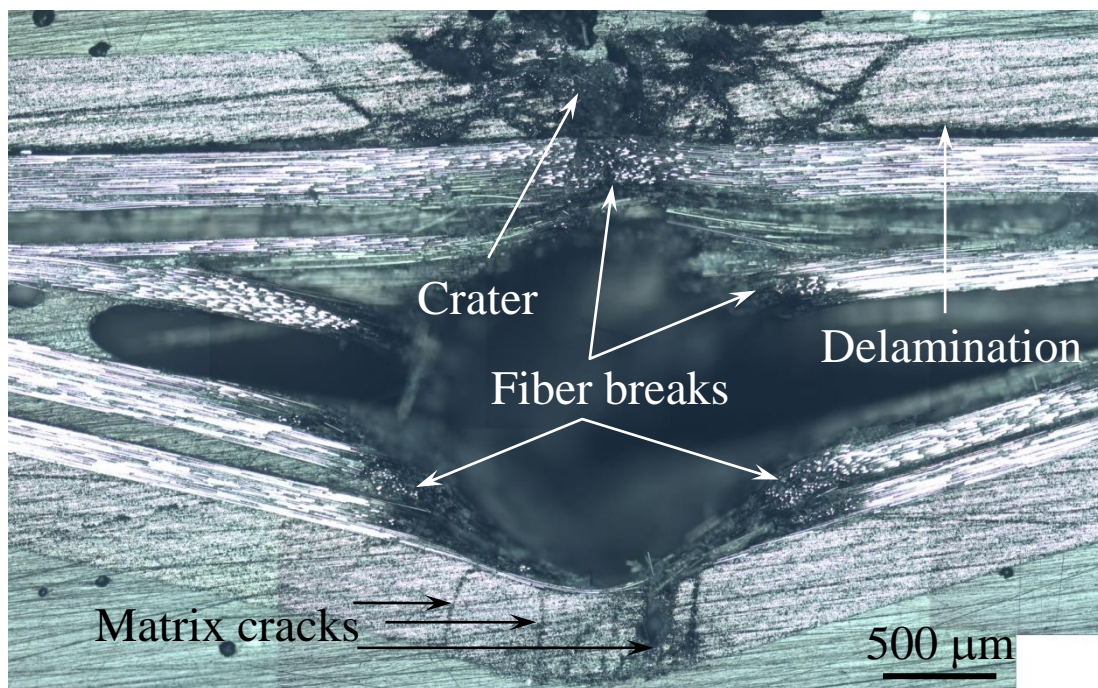
(d) CP1 (485 m/s) , Parallel to the 0° direction



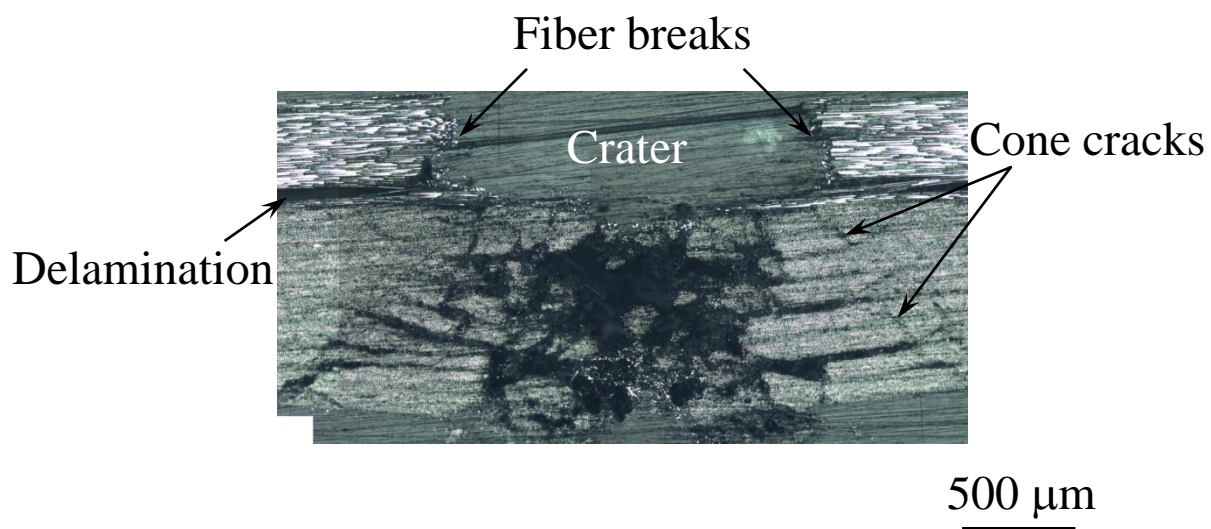
(a) Normal cross-section



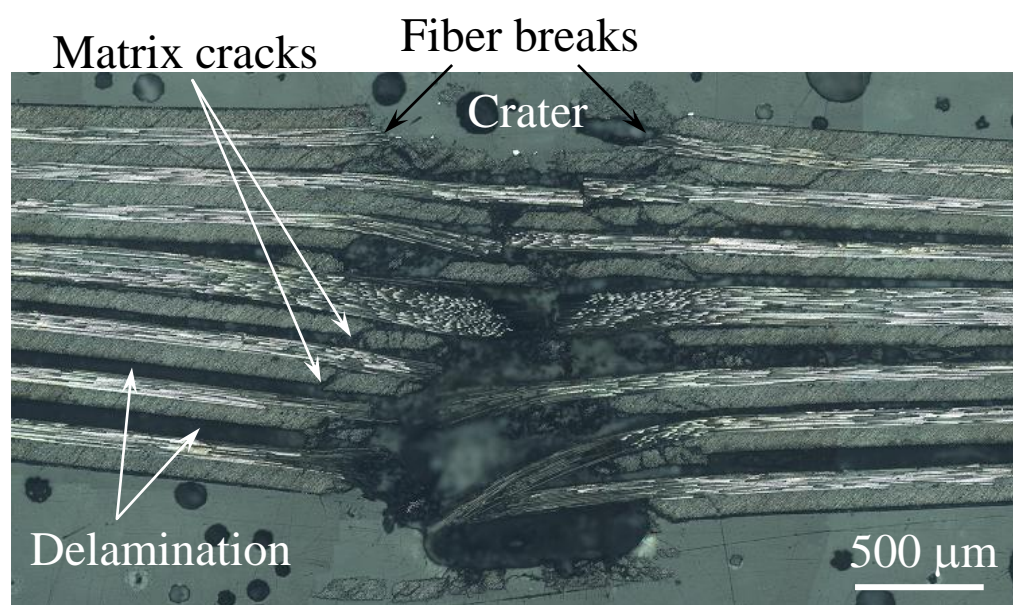
(b) Parallel cross-section



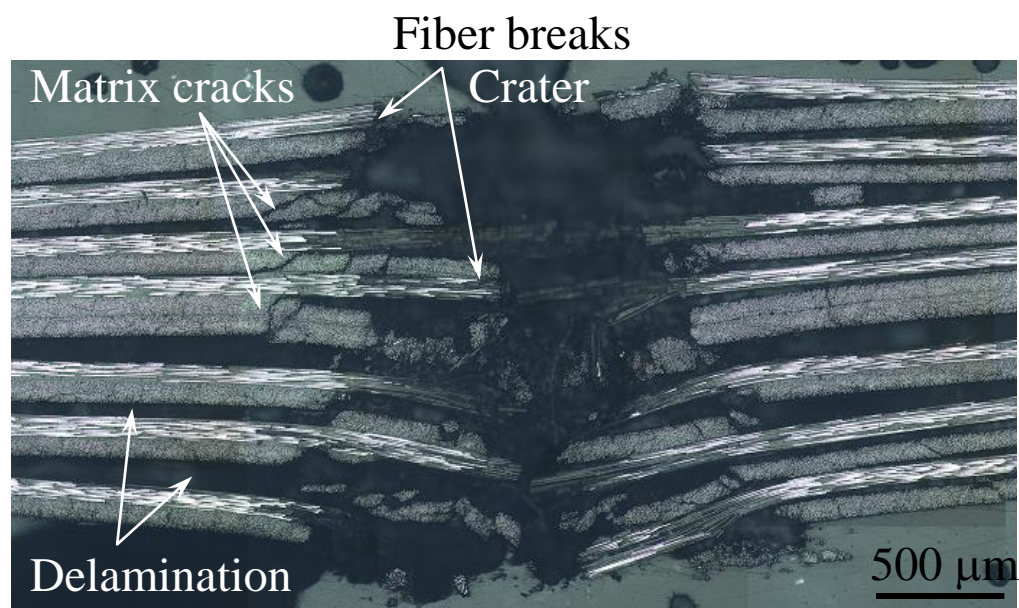
(a) Normal cross-section



(b) Parallel cross-section



(a) Normal cross-section



(b) Parallel cross-section

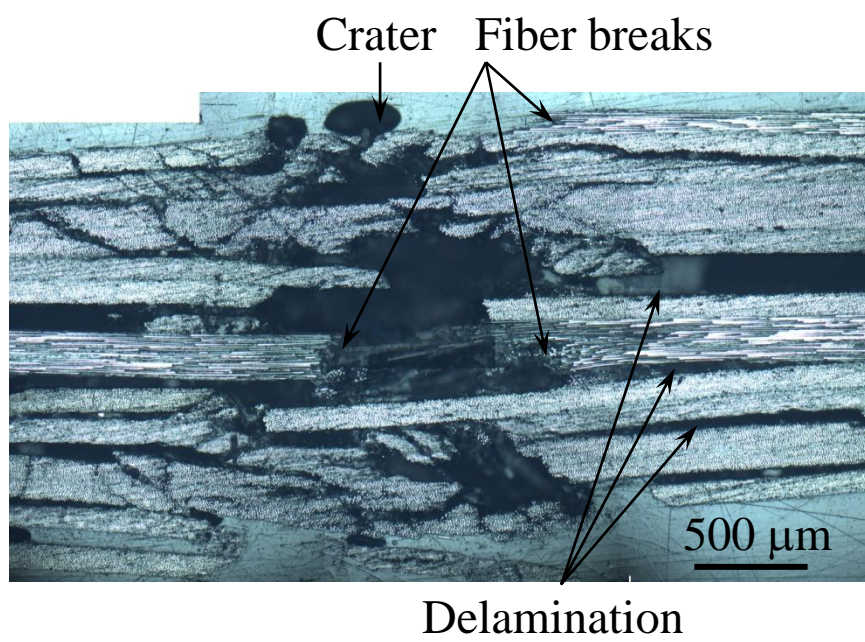
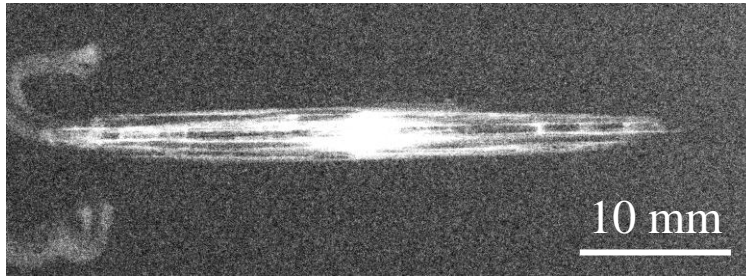
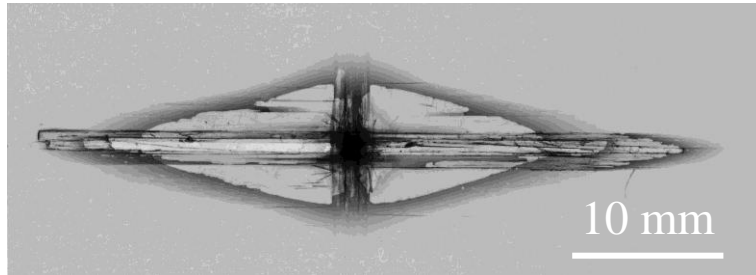


Fig. 11

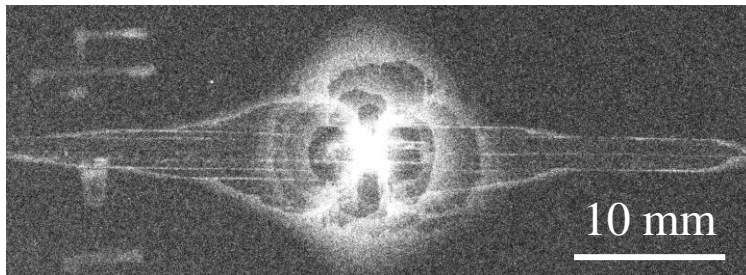
Fiber direction of 0° plies



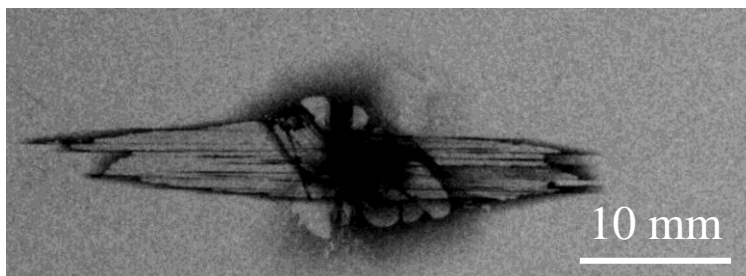
(a) UD laminate (506 m/s)



(b) CP1 laminate (485 m/s)



(c) CP2 laminate (500 m/s)



(d) QI laminate (560 m/s)

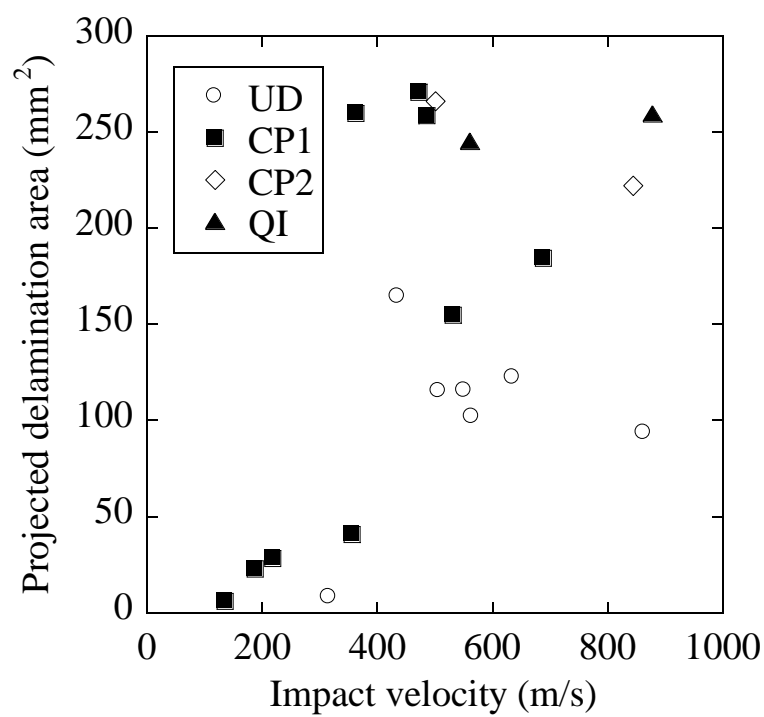


Fig. 13